

Additive manufacturing of compliance optimized variable stiffness composites through short fiber alignment along curvilinear paths

Torkan Shafighfard^{a,b}, Thomas A. Cender^{c,*}, Eralp Demir^{a,b}

^a*Faculty of Engineering and Natural Sciences, Sabanci University, Tuzla, 34956 Istanbul, Turkey*

^b*Integrated Manufacturing Tech. Research and Application Center, Sabanci University, Tuzla, 34956 Istanbul, Turkey*

^c*Center for Composite Materials, University of Delaware, Newark, DE 19716, USA*

Abstract

Short fiber-reinforcement has been used to improve the structural performance of extrusion based 3D printed polymer materials. The converging nozzle preferentially orients the short fibers along the printing direction. By locally steering the print paths to orient the fiber directions, the benefit of the anisotropic fiber reinforcement can be optimized. In this study, a methodology is developed to design and manufacture 3D printed short fiber-reinforced composite materials with optimized fiber or print directions. The standard open-hole tension sample geometry was employed as a test case. The least squares & continuity constraints (LSC) method was used to design the locally varying fiber orientation of each ply/layer to optimize for minimum compliance. An algorithm was developed to convert optimum discrete fiber angles to continuous paths. Material properties were estimated based the measured the fiber orientation tensor in conjunction with the Halpin-Tsai homogenization method. Strain measurements on open-hole tensile specimens by digital image correlation (DIC) were in good agreement with finite element model predictions. Despite some defects at path drop offs, LSC optimized samples showed improved stiffness and strength over zero degree orientation samples. In addition, samples prepared with print paths following streamlines for potential flow over a cylinder yielded higher strength and stiffness.

Keywords: Short Fiber Composites, Fiber Orientation, Design Optimization, Variable Stiffness Composites, Open-Hole Tension

*Corresponding author

Email address: tcender@udel.edu (Thomas A. Cender)

1. Introduction

Additive Manufacturing (AM), or 3D printing, is becoming more prevalent in industrial applications such as aerospace, automotive, construction and biomedical for fabrication of specialized parts, particularly with complex geometries. AM offers superior design flexibility in comparison to conventional manufacturing methods—thereby providing an opportunity to improve structural performance [1, 2].

Fused Filament Fabrication (FFF) is one of the commonly used, low cost and easily accessible AM techniques [3, 4], well suited for fabricating thermoplastic materials [5, 6, 7]. In this process, a continuous filament of material is extruded and deposited along 2D paths in order to build up a layer thickness [8, 9, 10]. A full range of thermoplastic materials can be used with FFF process, from common applications (PLA, ABS, PET) to high performance applications (PC, PEI, PEKK, PEEK). As with most AM processes, FFF provides lower mechanical performance than conventional industrial processes (such as injection molding) [11]. Deposited filament has limited adhesion to the substrate layer and less adhesion with adjacent filaments. Furthermore, the rounded geometry of deposited filaments creates a natural continuous porosity along the print paths. Due to the adhesion and porosity issues, FFF manufactured parts have intrinsic anisotropy. Print path (or raster) orientation, pattern, and width will dictate the tensile, flexural, failure, toughness of the 3D printed specimens [12]. Therefore, there is a great demand to improve mechanical properties, either by material and process optimization [13, 14] or by design optimization [15, 16, 17].

Fiber reinforcement, either short or continuous fibers, can be included in the FFF process to enhance mechanical properties [18, 19, 20]. The addition of short fiber-reinforcement, like in injection molding, is attractive because it requires little to no modifications of the existing process equipment [21]. Short fibers can be added directly to the polymer filament with minimal processing issues to yield substantial improvement in mechanical properties [22, 23]. During extrusion based AM, fibers align themselves along the print direction as they are extruded through the nozzle [24]. The result is the unique ability to produce highly aligned short fiber composite structures. Fiber alignment is highly desirable because the properties of the composite are much greater than randomly oriented fiber composites. This has motivated the fine tuning of properties of 3D printed materials by vary-

ing the fiber orientation during printing to increase the damage tolerance [25].

Variable stiffness (VS) composite laminate design is a technique to structurally optimize composite materials by steering fiber paths—contrary to traditional designs in which fiber directions are parallel and constant in each layer. This technique was developed for the Automated Fiber Placement (AFP) process, where a robotic arm steers fiber tows along computer controlled paths [26]. Likewise, other AM techniques, such as tailor woven composites (a stitching technique) [27] and extrusion based AM methods [28], have been used to manufacture VS composite laminates. To design a VS composite laminate, the local fiber orientation must be determined by an optimization routine in order to maximize structural performance based on the part geometry, loading conditions, and boundary conditions [29]. For an anisotropic material, the idea is to maximize loading in the highest strength (fiber reinforced) material direction while minimizing the stress in the weaker (transverse) material direction. Since both the fiber reinforcement and raster angles contribute to anisotropy of extrusion based 3D printed parts, this process is an ideal manufacturing process to apply VS design optimization.

Variable stiffness design has shown to be effective in a variety of structural composite material applications. Decreasing stress around holes and cutouts in composite plates and cylinders has considerable importance in aerospace applications; VS laminate design around fuselage windows is an active area of interest [30, 31]. The strength and stiffness of tailor woven "stiffness optimized" open-hole coupons showed an increase of 118% and 8% respectively relative to constant stiffness rectilinear composite laminates [32]. Similarly, single and double shear bearing capacity showed an increase of 29% and 63% respectively, compared to constant stiffness composites with drilled holes [27]. VS design has also proven effective in increasing bending stiffness [33], and the critical buckling load of composite shells [34] and cylinders [35]. Variable fiber volume fraction can be combined with variable fiber orientation to expand the parameter space for variable stiffness composite design. A recent study showed a 25% improvement in the ultimate load carrying capacity of VS over constant stiffness design [36].

A number of strategies exists for developing variable stiffness laminate design [37]. The challenge has two fronts: Fiber angles for optimal structural perfor-

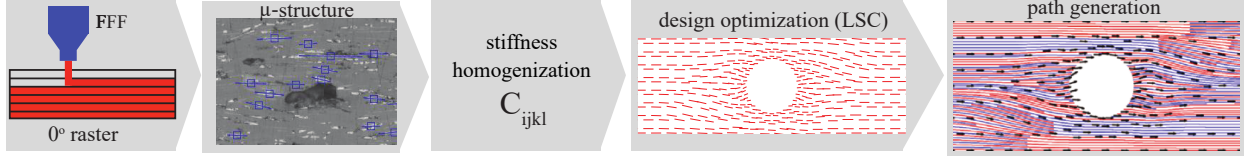


Figure 1: Schematic of the methodology used to obtain elastic properties from the process induced micro-structure and design/manufacture short fiber-reinforced composite structures.

mance must be solved for, and the fiber angles must constitute a manufacturable lamina—i.e. fiber angles must be interpolated into tool paths and those paths must be consistent with the steering limits for that material. In the AFP process, fixed width fiber tows have a path steering limit which corresponds to a minimum radius of curvature before the fibers begin to wrinkle [38]. This curvature constraint varies between materials and processes, but any VS design solution must have smooth curvature constrained tool paths. In some studies, stream functions were used to define fiber/tool paths [39, 40]. A more common approach is the interpolate tool paths (usually with splines) from discrete fiber angles at nodal points [41]. Demir et al. developed a design optimization approach called LSC (Least Squares & Continuity Constraints) in which optimum fiber directions were obtained in the form of discrete fiber angles [42]. Based on the curvature constraints of the given process and material, the fiber angles are adjusted relative to the exact optimum solution in order to trade-off performance with manufacturability. This approach requires an additional path generation strategy. Although, these techniques were originally developed for the AFP process, in which tow steering radius is extremely restricted (greater than 300-500 mm, [38]), the same design methods are applicable to extrusion based AM processes like FFF where constraints on print paths are lower.

Just as in high performance continuous fiber composite laminate structures, 3D printed materials (either metal [43] or polymer [44]) have directional (anisotropic) properties which can be both detrimental and exploitable. Historically, laminate design for continuous fiber composite materials, and more recently extrusion based 3D printed structures, have tried to suppress the weaker material directions by employing quasi-isotropic stacking sequences. With the implementation of robotic material deposition processes, the ability to control material orientation has entered a new phase. Robust design of material orientation and its implementation and effectiveness in manu-

facturing processes must be developed in parallel in order to achieve the full potential of robotic additive manufacturing.

In this study, a methodology is developed for the design and manufacturing of aligned short fiber reinforced variable stiffness parts for FFF 3D printing. Fig. 1 shows a schematic of the proposed method. A short carbon fiber filled (20% by volume) Polyethylene Terephthalate Glycol-Modified (PETG) filament was selected to produce samples using a desktop 3D printer. A standard open-hole tensile geometry [45] was used for VS design optimization and experimental validation to show performance improvement over a conventional print path strategy with constant stiffness design. Filament scale anisotropy was determined by measuring the short fiber orientation within an extruded filament. The lamina stiffness tensor was evaluated by using Halpin-Tsai relation for short fiber-reinforced composites in conjunction with the measured fiber orientation tensor. From the anisotropic material stiffness tensor, the local fiber angles which produced the minimum compliance specimen were solved for with the LSC design optimization method. Discrete angles were extrapolated to continuous print paths and converted to g-code for manufacturing with 3D printing.

Open-hole tensile specimens, tested and analyzed with Digital Image Correlation (DIC), show that stress concentration in LSC samples were distributed more homogeneously around from hole relative to constant stiffness samples with 0° raster angle, thereby increasing the tensile strength. For comparison, VS samples were also prepared with print paths following streamlines for potential flow around a cylinder. The streamline design yielded the highest ultimate strength and stiffness despite greater variability.

2. Methodology

Sections 2.1 and 2.2 describe the test sample geometry and the material types that are used in this study. Section 2.3 explains the micro-structural anal-

ysis and the Halpin-Tsai homogenization method to obtain the overall elastic properties of a 0° laminate. Section 2.4 briefly describes the design optimization method (LSC) to find the fiber angles for optimum structural compliance as well as a print path design based on streamlines for potential flow around a cylinder. Section 2.5 shows the path generation method that was used to convert of discrete angles from the LSC design to continuous print paths. Section 2.6 describes the methods that are used for the manufacturing by 3D printing. Section 2.7 explains the experimental validation techniques.

2.1. Test sample geometry

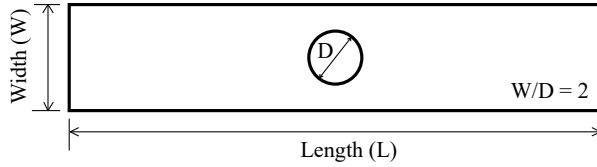


Figure 2: Schematic sketch of the sample with hole

ASTM D5766 [45] was followed to design and manufacture open-hole tensile specimens (shown in Fig. 2). A sample width to hole diameter ratio of two ($W/D=2$) was selected. A specimen geometry of $L = 150\text{mm}$, $W = 25\text{mm}$, and $t = 2.0\text{mm}$ (thickness) was chosen.

2.2. Material types

ColorfabbTM XT was selected as the filament polymer material. Samples were prepared from both XT (pure PETG polymer) and XT-CF20 filament, which has 20% fiber volume fraction of short carbon fibers with an average fiber length less than 0.15 mm.

2.3. Microstructural Analysis

Specimens were 3D printed from the short fiber filled filament along 0° raster paths to produce samples for micro-structural analysis to identify the filament scale fiber orientation. Specimens were polished and analyzed with optical microscopy in order to determine the fiber angles and the their distribution. All of the samples were ground with the 600 grit silicon carbide paper followed by the 1200, 2000, and 4000 grit papers in order to provide smooth surface

to capture the high quality figures under the microscope. A Nikon-lv150 microscope was used to capture the optical micro-graphs shown in Fig. 3.

The short fibers, which orientate themselves in the print direction during the printing process, cause filament scale anisotropy. Fig. 3(a) shows longitudinal section of two printed filaments where short fiber reinforcement is highly aligned with the filament extrusion direction, and fibers are well distributed throughout the entire filament cross-section. Fiber alignment (shown clearly in Fig. 3(b)) is not perfect due to insufficient relaxation time for fibers to rearrange themselves while passing from the nozzle [46].

An image processing script written in Matlab[®] was used to find the position and orientation of fibers. Fig. 3(b)) shows a blue square marker and line overlaying a set of fibers to denote their centroid and orientation determined from image processing. Fig. 3(c) shows a histogram of fiber angles (relative to the print direction) for 164 fibers analyze by image processing. It was determined that the filament scale representative volume element has $\sim 18\%$ porosity due to empty channels which follow filament paths.

The Advani-Tucker fiber orientation tensor [47] was used to evaluate the averaged filament scale properties due to the presence of short fibers. Second and fourth order fiber orientation tensors were calculated directly from the discrete set of fiber angles obtained by image processing. The orientation of each fiber is represented as a unit vector $\mathbf{p} = \langle \cos(\theta), \sin(\theta), 0 \rangle$. The averaged second order orientation tensor, A_{ij} (Eq. 1a), and fourth order orientation tensor, A_{ijkl} (Eq. 1b), were computed by summation rather than computing and integrating the continuous probability distribution function, $\psi(\theta)$. The superscript n represents the n^{th} fiber of the total set $N = 164$.

$$A_{ij} = \int_{-\pi/2}^{\pi/2} p_i p_j \psi(\theta) d\theta \approx \frac{1}{N} \sum_{n=1}^N p_i^n p_j^n \quad (1a)$$

$$A_{ijkl} \approx \frac{1}{N} \sum_{n=1}^N p_i^n p_j^n p_k^n p_l^n \quad (1b)$$

From the micro-structural measurements, the second order fiber orientation tensor was found to be

$$A_{ij} = \begin{bmatrix} 0.988 & 0 & 0 \\ 0 & 0.012 & 0 \\ 0 & 0 & 0 \end{bmatrix}$$

, where the component, A_{33} , was neglected because

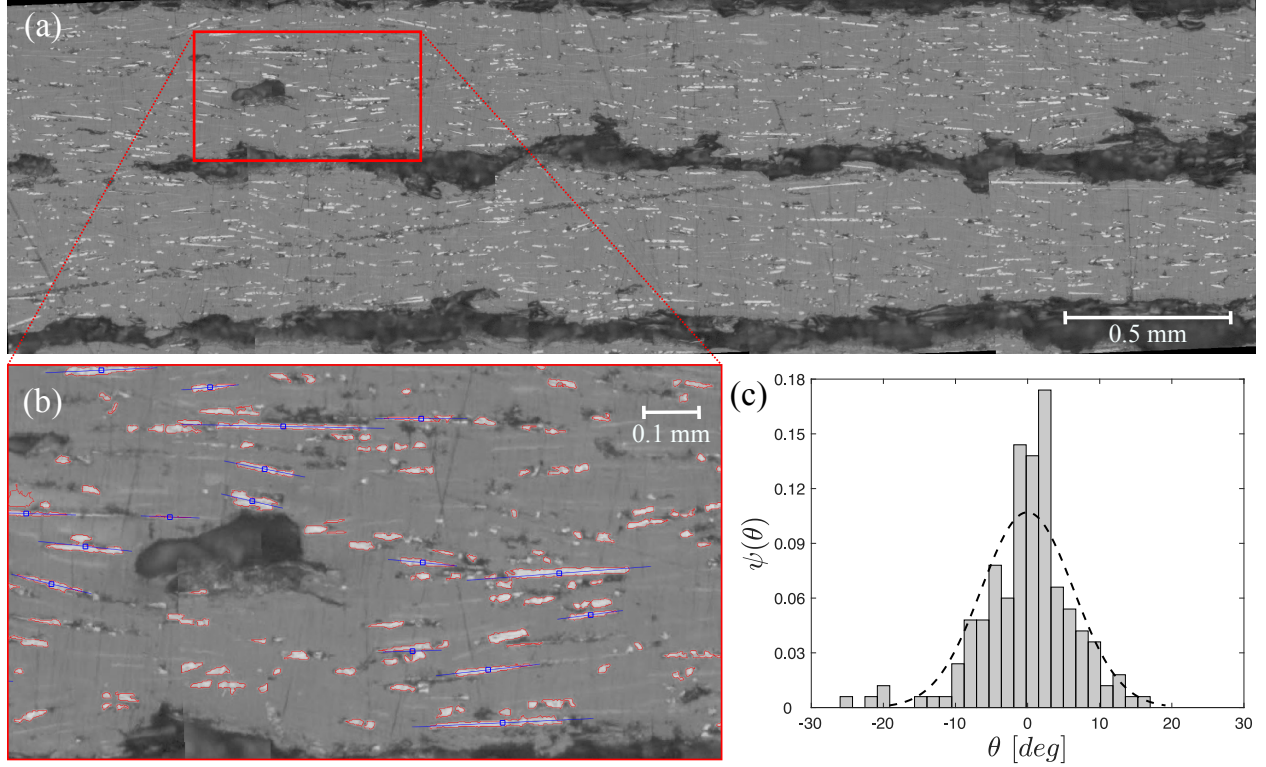


Figure 3: Filament scale fiber orientation was determined from optical micro-graphs of a polished sample. (a) Micro-graphs of polished printed filaments were obtained to observe the fiber distribution along the filament length. (b) Blue marker and lines are overlaid on this magnified view to show the fiber centroid and primary axis. (c) A probability density distribution, $\psi(\theta)$, vs. fiber angle (θ) was determined from a set of 164 fibers.

the out-of-plane fiber orientation is not measurable by optical microscopy. An assumption about the out-of-plane orientation could be made from the in-plane orientation, or it could be measured directly from x-ray micro-ct 3D reconstruction; however, due to the high fiber alignment observed in Fig. 3, the effect on the results is not significant.

The Halpin-Tsai model defines the averaged elastic stiffness tensor C_{ijkl} for perfectly aligned short fibers based on the fiber aspect ratio and volume fraction [48]. The elastic stiffness can be transformed for the case of non-aligned fibers based on the Advani-Tucker averaged fiber orientation tensor [47].

The composite material is considered as a set of equivalent representative volume elements (RVE) such that the fibers are well mixed without any short-range ordering or local domain structure. Each RVE has its own fiber alignment based on the fiber orientation tensor. The stiffness of the composite is calculated by transposing the stiffness tensor of the homogenized RVE for each finite element. The averaged stiffness

tensor is computed by Eq. (2) [47].

$$C_{ijkl} = B_1 A_{ijkl} + B_2 (A_{ij} \delta_{kl} + A_{kl} \delta_{ij}) + B_3 (A_{ik} \delta_{jl} + A_{il} \delta_{jk} + A_{jl} \delta_{ik} + A_{jk} \delta_{il}) + B_4 \delta_{ij} \delta_{kl} + B_5 (\delta_{ik} \delta_{jl} + \delta_{il} \delta_{jk}) \quad (2)$$

Stiffness tensor multipliers, B_i , are calculated from stiffness constants from the Halpin-Tsai model, Eq. (3).

$$\begin{aligned} B_1 &= C_{11} + C_{22} - 2C_{12} - 4C_{66} \\ B_2 &= C_{12} - C_{23} \\ B_3 &= C_{66} + \frac{1}{2}(C_{23} + C_{22}) \\ B_4 &= C_{23} \\ B_5 &= \frac{1}{2}(C_{22} - C_{23}) \end{aligned} \quad (3)$$

C_{11} , C_{22} , C_{12} , C_{66} , C_{23} are the coefficients of the elasticity tensor which are calculated using the elastic constants of the short carbon fiber-reinforced lamina, i.e. the longitudinal (E_{11}), transverse (E_{22}), in-plane shear (G_{12}), out-of-plane shear (G_{13}) moduli

and Poisson's ratio (ν_{12}).

Table 1: Fiber and matrix properties of the short fiber-reinforced composite material.

l/d	V_f	E_m (GPa)	E_f (GPa)	ν_m	ν_f
8	0.2	1.8	190	0.3	0.2

Elastic coefficients are obtained by using the fiber and matrix properties that are shown in Table 1, in accordance with the homogenization scheme shown in reference [49]. For simplicity, the fibers are assumed to be isotropic. Although carbon fibers are transversely isotropic, this assumption is efficient because the filament is relatively low fiber volume fraction—the aligned fiber composite stiffness is dominated by the polymer matrix. For advanced applications, a theoretical framework should be applied which accounts for transverse isotropy of the polymer and carbon fiber phases [48, 50, 51].

2.4. Design optimization: Least-Squares & Continuity Constraints (LSC)

The LSC technique was developed in order to design VS optimized laminate structures which are manufacturable with the constraints of the AFP process [42]. The advantage of this optimization approach is that it requires no prior assumptions for the fiber angle distributions, e.g. the spline functions, fluid potentials, etc. In the objective function, compliance and lamination parameters are used as design variables to perform convex optimization. The fiber angles and stacking sequence of each layer have to be identified after the optimization process from the optimum lamination parameters. The optimum fiber angles are then used to find the fiber angle distribution throughout each lamina of the sample. The LSC method has shown to be effective for VS design for shell structures and the compliance optimization also helps to reduce the stress concentration around various types of holes [52].

The LSC method contains two constraints that trade off the optimum solution for fiber angle distribution with the local continuity of fiber angles. The purpose of this approach is to design with a smoother and more continuous fiber angle distribution than the optimum fiber angle distribution, $\theta_{opt}(x, y)$, that reveals the minimum compliance. The material properties computed from the Halpin-Tsai homogenization method in Section 2.3 are used to solve for $\theta_{opt}(x, y)$. Considering the limitations of manufacturing process

(local path curvature), a search is performed for a fiber angle field distribution, $\theta(x, y)$, which has the least different from the optimum, Eq. (4).

$$\theta(x, y) - \theta_{opt}(x, y) = 0 \quad (4)$$

To control the local continuity of fiber angles, the gradient is set to zero as in Equation (5).

$$\nabla\theta(x, y) = 0 \quad (5)$$

The local form of these constraints are expressed in global form to solve for the fiber angles. A penalty factor is used to tune these constraints in order to control the curvature. The minimum radius of curvature can be set to any value; in this study, it was set to the radius of the hole in the sample, R , of 6.25 mm. As mentioned in Section 1, the minimum tow steering radius is greater than 300-500 mm for the AFP process [38].

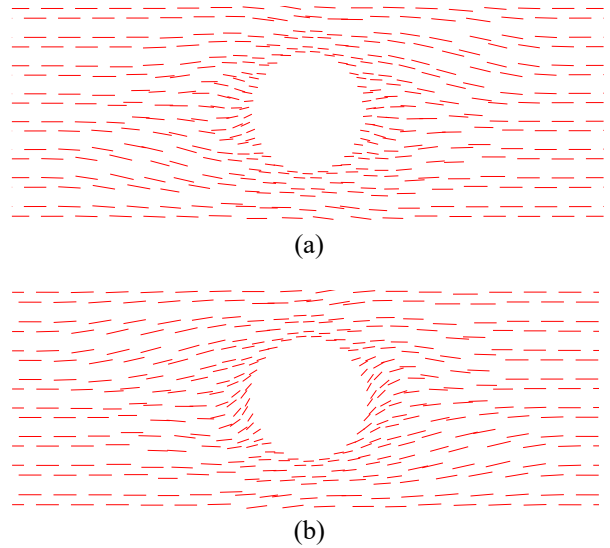


Figure 4: LSC solution for fiber angle distribution with radius of curvature constrained to 6.25 mm; (a) for first and fourth layer, and (b) for second and third layer of a four ply symmetric laminate.

Fig. 4 shows the LSC solution for the fiber angle distribution $\theta(x, y)$ around sample hole. This method provides the angles at the center of each element discretely; hence, a separate algorithm is required to connect these discrete angles to find continuous and manufacturable tool paths.

For the open-hole tension sample geometry, the LSC design reveals a 3.4% increase in stiffness and a 5.3% decrease in the stress concentration factor with

respect to the constant stiffness design with 0° fiber direction. The reduced stress concentration factor for the LSC design implies higher failure strength. Structural performance improvements are limited for the standard open-hole tension geometry with uni-axial loading; the benefits by employing the LSC method for VS design are much higher for more complex loads and/or more complex geometries [52].

2.5. Path generation

Two methods are implemented and compared for generating curvilinear print paths. To experimentally evaluate the performance of the LSC design optimization method, print paths were generated from the fiber angles at nodal points. In an alternative approach, print paths were generated from streamlines for potential flow around a cylinder. In both approaches, the width of print paths (filament deposition width) was allowed to vary along the path between 0.25-0.5 mm for a 0.5 mm diameter print nozzle. Print paths were generated from line segments produced by a Matlab script for extrapolating paths from fiber angles. The print paths were written into G-Code with the open source Mecom python library [53]. The Mecom library allowed for the filament width to be varied locally by adjusting the extrusion feed rate relative to the print head feed rate. With the layer height and nozzle diameter remaining constant, the volume of extruded material was consistent with the specified print width.

2.5.1. Continuous print paths from discrete angles from LSC design

An algorithm was developed in Matlab in order to generate continuous 3D printable paths from discrete fiber angles at nodal points from the LSC curvature constrained solution. The algorithm allowed for filament width to vary (within limits) along each print path and allowed paths to be selectively dropped or generated based on the divergence of vector field. The goal is to produce a set of paths with varying width (linearly discretized: x_i, y_i, w_i) which are parallel to the fiber orientation vectors and fill the entire area.

Fiber orientation values (θ) at nodal points (x, y) (from Fig. 4) were interpolated to a fine 2D grid in order to query an orientation angle at any point within the domain. Paths were initiated from seed points (x_0^k, y_0^k , where k is the line number) chosen along the mid-plane and following the edge of the hole—shown as blue circles in Fig. 5. From seed points,

all paths (black lines in Fig. 5) were extrapolated by an equal distance (Δx) in the direction of the local fiber orientation vector θ_0^k . The path width is calculated as the distance between adjacent paths. If the path width falls below the minimum printable threshold such that $w(x, y)^k$ is less than 0.25mm, then the path is terminated, as shown in Fig. 5 with a red "x". Likewise, if paths diverge such that the width, $w(x, y)^k$, increases above the maximum printable threshold of 0.5 mm, a new path is seeded, shown with a red "o" in Fig. 5. The extrapolation and interpolation processes is iterated until all paths are terminated by intersecting the domain boundary.

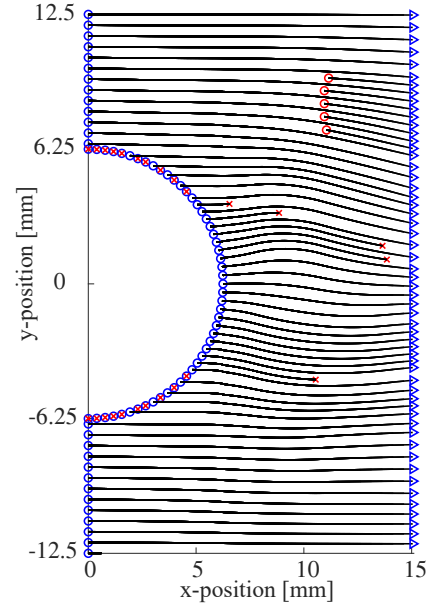


Figure 5: Depiction of how paths were spliced.

Fig. 6a shows how the path lines (in red and blue) fill the sample domain area and follow the orientation vectors (black arrows) from the LSC solution. Fig. 6b is an image of the bottom layer of a sample 3D printed with short carbon fiber filled filament from the path lines shown in Fig. 6a.

2.5.2. Streamlines from potential flow around a cylinder

An alternative strategy for implementing curvilinear fiber paths for a composite plate with a cut-out is to imitate the solution for potential flow around a cylinder [40, 54, 55, 56, 57]. Fiber print paths and path widths are derived to follow streamlines. This ensures perfect continuity around the hole and com-

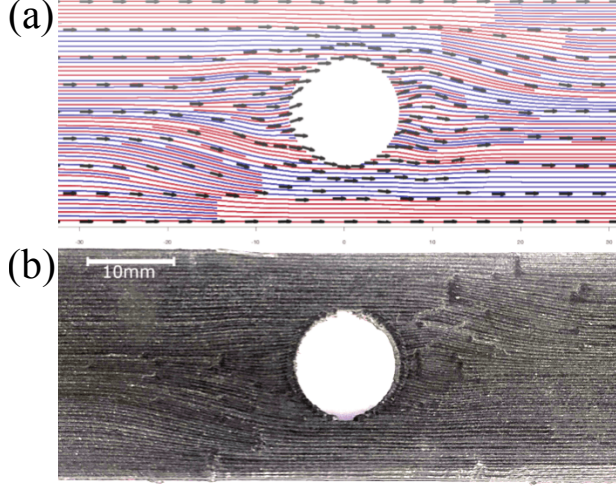


Figure 6: LSC design; (a) fiber paths, (b) printed sample. Only the 1st layer is shown for simplicity.

plete filling of the domain since conservation of mass is enforced in this solution.

The stream function for potential flow around a cylinder in polar coordinates (r, ϕ) as the superposition of a uniform flow over a doublet [58].

$$\psi = U_{\infty} \sin(\theta) \left(r - \frac{R^2}{r} \right) \quad (6)$$

In Eq. 6, U_{∞} is the far field velocity, and R is the radius of the cylinder.

Path lines are computed from the coordinates (x, y) which fall on streamlines, i.e. $\psi = C$, C being a constant. In order to compute the width of fiber paths, the velocity components are computed using Eqns. (7a) & (7b).

$$u_x = \frac{R^2(y^2 - x^2) + (y^2 + x^2)^2}{(y^2 + x^2)^2} \quad (7a)$$

$$u_y = \frac{-2R^2xy}{(y^2 + x^2)^2} \quad (7b)$$

Since mass flow rate along a streamline is constant, the distance between streamlines changes proportional to the velocity. Therefore, the path width can be derived from the magnitude of the velocity.

$$\dot{m} = |u(x, y)| w(x, y) = U_{\infty} w_{\infty} = C \quad (8)$$

A reference value for the nominal width of $w_0 = 0.4$ mm is set to correspond to the far stream velocity $|u_0| = U_{\infty}$. From that reference, the path width can

be computed at any point with Eq. (9).

$$w(x, y) = \frac{\dot{m}}{|u(x, y)|} = \frac{|u_0|}{|u(x, y)|} w_0 \quad (9)$$

Fig. 7 shows the the printed sample using the potential fluid flow concept in which the printed raster has varying width. At the top edge of the hole the velocity doubles, causing the path width to halve. At the stagnation point, the velocity approaches zero, which as seen in Fig. 7, results in path widths which the nozzle is not able to extrude. The unintended porosity near the stagnation point influences the strength and stiffness of the sample in an unknown way.

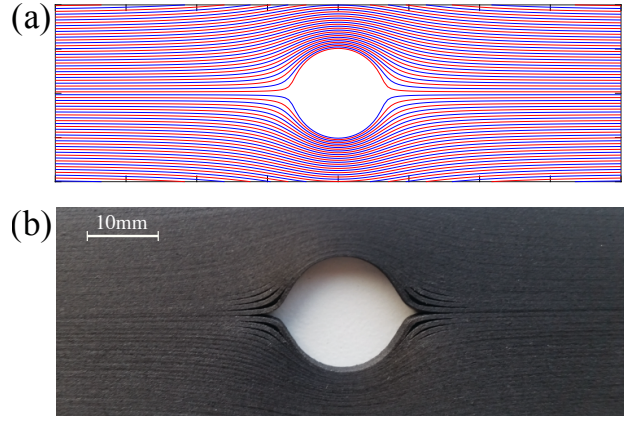


Figure 7: (a) Fiber paths based on streamlines for flow over a cylinder. (b) Carbon fiber-reinforced printed sample.

2.6. Manufacturing by 3D printing

Samples were fabricated with a Creality CR-10S 3D printer—shown in Fig. 8. Table 2 shows the manufacturing process and design parameters, which were the same for all the specimens. All samples consisted of 10 layers to obtain a total thickness of 2 mm. A batch of five samples for each specimen type were fabricated and tested for repeatability.

The feedstock material was a 1.75 mm diameter filament. For the material without fibers (w/o fiber) a 0.4 mm diameter nozzle was used, while a 0.5 mm diameter nozzle was used for the short carbon fiber-reinforced material. The larger diameter nozzle helped to avoid clogging with the carbon fiber filament. Also, it was observed that the carbon fiber filament was not able to over-extrude well due to its increased viscosity; therefore, variable filament width was achieved by under-extruding.

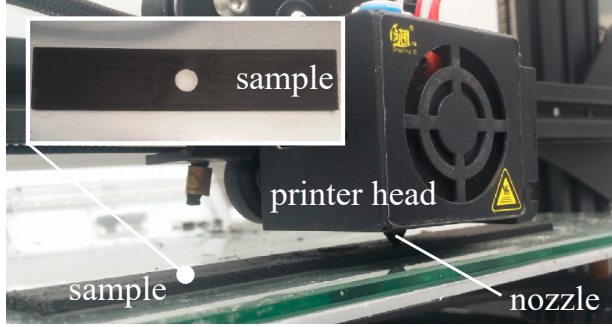


Figure 8: 3D printing system during carbon fiber-reinforced sample

Table 2: Manufacturing parameters used for printing the carbon fiber-reinforced samples in the 3D printing process.

Parameter	Value
Material	ColorFabb XT & XT-CF20
Filament diameter	1.75 mm
Nozzle diameter	0.5 mm
Nozzle temp.	260 °C
Build plate temp.	80 °C
Cooling	Fan (35%)
Layer height	0.2 mm
Number of layers	10
Printing speed	8 mm/s
Retraction	5 mm
Build plate adhesion	4 mm Brim
Path generation	Custom algorithm
G-code generation	Python (Mecode [53])

Manufacturing parameters were selected to minimize the printing defects. For example, eight brim filaments were used in order to avoid delamination of the sample from the print bed. For print paths that encounter an unavoidable discontinuity (due to path terminations), the filament is retracted and the print head jumps to start the next path. A brush is set up next to the part in order to clean the printer nozzle periodically after finishing each layer to prevent the material jamming inside the nozzle.

2.7. Experimental validation

To validate the design approach and model results of the LSC technique, 3D printed open-hole samples were tested in uni-axial tension and observed with Digital Image Correlation (DIC). Five specimens were prepared to identify experimental variation to ensure the repeatability. Stiffness, strength,

toughness, and failure strain are reported for all the specimens.

An Instron universal testing system with a 0.5 kN load cell was used to measure load-displacement curves. A 100 mm gauge length is used to convert the displacements to strains. Tensile tests were performed with the strain rate of 2.2×10^{-4} 1/s. LSC designed specimens and specimens with a 0° raster angle were analyzed using a GOM ARAMIS 5M DIC system to obtain surface strain maps. Speckle patterns were applied to the samples with spray paint: a white background with black speckles. Figure 9 shows the experimental setup with the DIC camera, load frame, and test sample. Bi-axial strain gauges were used to determine the elastic constants of printed samples without holes (shown in Table 3).

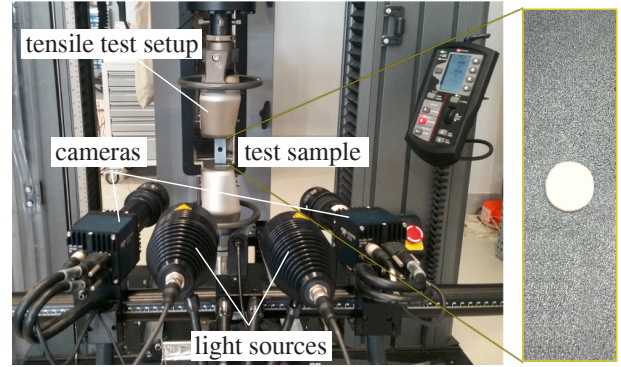


Figure 9: DIC cameras and load frame coupled with painted test sample

3. Results and discussion

Samples without holes (0° , 90° , and $\pm 45^\circ$ raster angles) were fitted with bi-axial strain gauges and tested in tension in order to determine the elastic constants: longitudinal, transverse, and shear modulus as well as Poisson's ratio. The same properties were calculated based on analysis of a specimen with 0° raster angle by using the Halpin-Tsai relation with the fiber orientation tensor that was obtained from image analysis. Table 1 shows modulus of elasticity and Poisson's ratio of the fiber and matrix material used in this study. The measured and calculated stiffness constants are in agreement ($\sim 12\%$ error), as shown in Table 3. The lower modulus values reported for the experimental samples are quite expected: manufacturing defects (e.g. porosity from 3D printing) and fiber variations (length, strength, and end effects) can account for up to a 20% reduc-

tion in properties [59]. Porosity was measured to be $\sim 18\%$, and is very close the experimentally observed difference in the longitudinal elastic modulus of approximately 13.1%.

Fig. 10 shows the stress-strain curves for the two sets of samples for each case. Five samples for each case were tested but only two of each sample type (maximum and minimum cases) are shown in the figure for clarity.

Table 3: Elastic constants of the short carbon fiber-reinforced lamina of experimental and theoretical values using the Advani-Tucker homogenization method.

	E_{11} (GPa)	E_{22} (GPa)	ν_{12}	G_{12} (GPa)	G_{23} (GPa)
experimental	6.676	2.328	0.38	0.948	0.843
theoretical	7.55	2.42	0.28	0.80	0.74

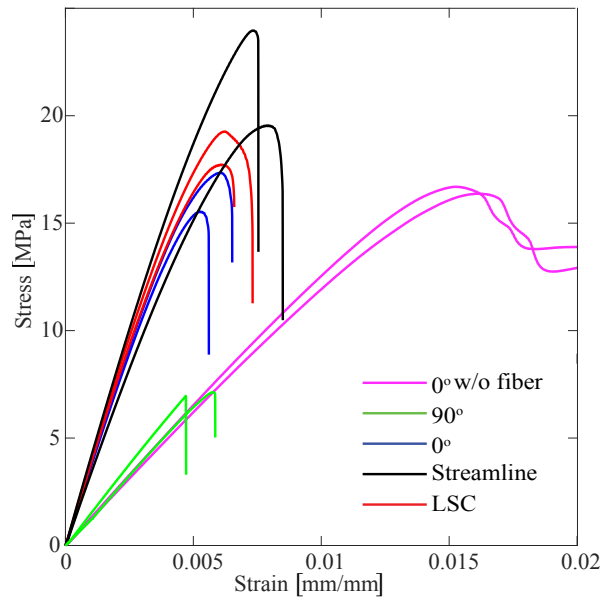


Figure 10: Experimental stress-strain curves for open-hole specimens. The two of the most different experimental results out of five tests are shown only for clarity.

Fig. 11 shows images of each type of specimen after failure. Samples failed at the narrowest cross-section where the stresses are highest, as expected. The 0° raster angle specimens (both with and w/o fiber-reinforcement) had a less definite fracture surface since the structure and stresses are both uniform near the hole over a wider region making the failure to occur non-uniformly. This can be validated using the strain measurements in Fig. 13. Another interesting observation was the failure of the sample

with 90° raster angle. One of the failure surface was along the raster direction showing the effect of voids that are continuous along the raster (print) direction. The streamline design had approximately 40% higher failure strain than LSC and 0° specimens. LSC designed specimens had a uniform failure surface which was well defined at the location with highest strain.

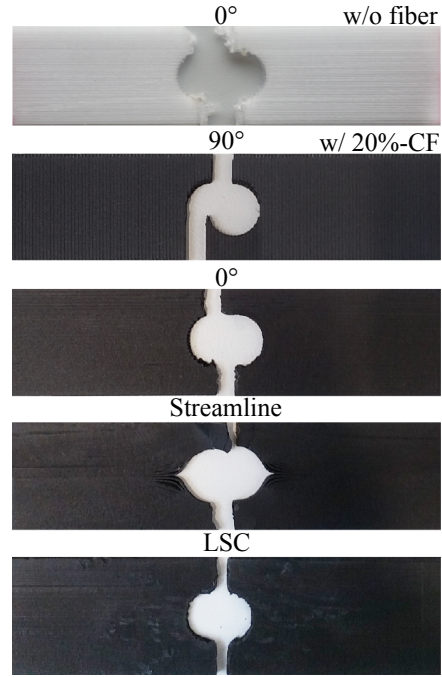


Figure 11: Samples after failure. All fractures initiated at mid-plane adjacent to the hole.

Fig. 12 and Table 4 show the overall results collected by the mechanical tests. Open-hole samples types having short carbon fiber filled filament include pure 0° raster angle, pure 90° raster angle, LSC optimized VS design with a minimum radius of curvature of 6.25 mm, and samples fabricated from the fluid flow analogy (streamlines for potential flow around a cylinder). The samples with 90° raster angle had the lowest stiffness and strength as expected; not only were the sample loaded transverse to the fiber orientation, but the porosity and adhesion between adjacent filaments is known to be poor.

LSC designed VS specimens, had the highest average stiffness, with a Young's Modulus of 3.83 GPa–3.6% more than the samples with 0° raster angles. This increase is in agreement with the finite element findings which predicted a 3.4% increase with the LSC optimization for minimum compliance. The LSC specimens also showed an increased strength by 5.4%

with respect to the specimens with 0° raster angle. The increased strength is due to a reduced stress concentration factor around the hole due to the variable stiffness design.

The streamline specimen revealed a significantly better failure strength improvement: a 20% increase over the LSC design. This streamline pattern produced superior path continuity relative to what was achievable with this LSC design. As shown in Fig. 5, while printing the LSC design, print paths had to be terminated at many locations—both within the sample as well as on the hole boundary. At these path terminations the nozzle had to stop, retract the filament, lift off the path and translate to start a path at a new location. At each path discontinuity there is no fiber alignment and there is a higher probability of introducing porosity. These interruptions to printing results in visible defects which can be seen in Figs. 6(b) & 11. Manufacturing defects likely led to a lower resistance to failure for the LSC designed samples. The effect of increased material porosity in the streamline specimen near the ‘stagnation point’ is not clear. It likely contributed to a decreased sample stiffness and increased failure strain (by allowing the sample to neck), but would not increase the strength for any obvious reason.

Fig. 13 shows the in-plane strain fields (ϵ_{xx} : strain in direction of loading) from Digital Image Correlation (DIC) for 0° and LSC specimens at four different load points along to stress-strain curves. The strain map reveals the classical strain pattern in the vicinity of a hole. Comparison of the experimental results shows that strain is more evenly distributed in the LSC sample. In the 0° sample, strain is highly concentrated in the regions adjacent to the hole at the mid plane ($x = 0$ with the axis origin at the center of the hole) and extends towards the top and bottom end of the sample. A similar pattern is observed in the LSC sample; however, the magnitude of strain adjacent to the hole (at $x = 0$) is lower and the highly strained region extends further away from the hole in the x-direction. As the high strain region extends away from the hole, the average strains become more homogeneously distributed along the vertical edges of the sample. These experimental results are in good agreement with the finite element analysis results, which predicted a stress concentration factor of 3.75 and 3.55 for the 0° and LSC samples, respectively.

The variable stiffness design provided by the LSC technique was successfully able to make use of the anisotropy of the material in order to redirect stress

around and away from the hole. The curvature constraint of LSC design converts optimum variable stiffness fiber angle distribution maps into smooth and manufacturable 3D print paths. In this application, curvature of the print paths could still be increased further while maintaining good filament scale fiber orientation; however, tighter curvatures lead to less continuous fiber angle maps, which create a greater number of path discontinuities.

4. Conclusions

In this study, a methodology is developed to design and manufacture variable stiffness (VS) laminate structures. Filament scale properties were analyzed with optical microscopy in order to obtain the averaged fiber orientation tensor. The elastic properties fiber and matrix constituents are used in conjunction with Halpin-Tsai method and fiber orientation tensor to compute the homogenized properties of an RVE. From the measured material properties, the LSC method was used to determine curvature constrained, manufacturable fiber angles which optimize for minimum compliance. Fiber angles at discrete nodal points were sliced to produce continuous print paths which were converted to g-code in order to manufacture tensile specimens. The LSC method was applied to an open-hole tensile geometry with standard dimensions, and was compared specimens with 0° raster angles and specimens designed from streamlines for potential flow over a cylinder.

Variable stiffness design using LSC method showed improved stiffness and tensile strength in comparison to samples with 0° raster. The LSC fiber angle distribution and path slicing algorithm resulted in defects occurring at print path terminations. Compared to 0° raster specimens, DIC results showed that the LSC design produced a more uniform distribution of strain around the hole. Despite more local defects, LSC samples had a higher tensile strength due to a lower strain concentration in the vicinity of the hole.

Samples fabricated using the streamline design had the best tensile strength and stiffness but a larger scatter exists in the experimental findings. It’s unclear exactly why the streamline design performed so well, but the continuity of print paths and porosity near the stagnation point like had an important role in its greater failure resistance.

The benefits of variable stiffness design becomes more apparent as the part geometry, boundary conditions, and loading become heterogeneous [52]. The

Table 4: Mechanical properties for all of the test cases.

	short fiber-reinforced					w/o fiber	
	w/o hole 0°	90°	0°	Streamline	LSC	w/o hole 0°	0°
Stiffness (GPa)	5.3	1.4	3.70	3.59	3.84	1.6	1.2
Strength (MPa)	51.2	6.5	16.8	21.3	17.8	43.7	16.4
Toughness (j.m^{-3})	1.013	0.016	0.065	0.100	0.075	1.343	0.287
Failure strain (mm/mm)	0.022	0.004	0.005	0.007	0.005	0.045	0.015

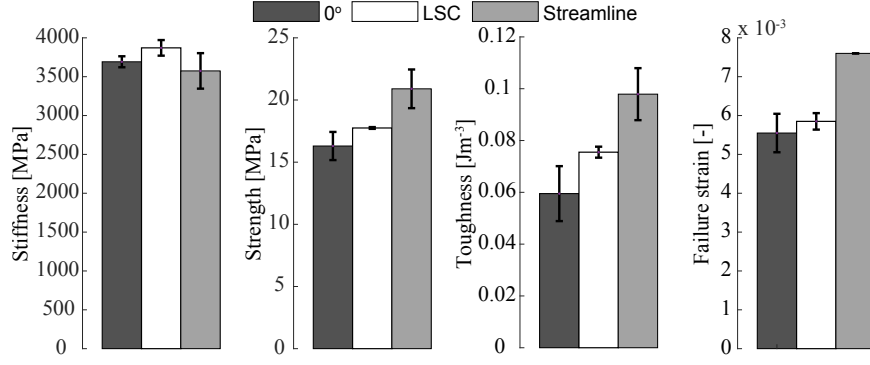


Figure 12: Mechanical properties for all design cases.

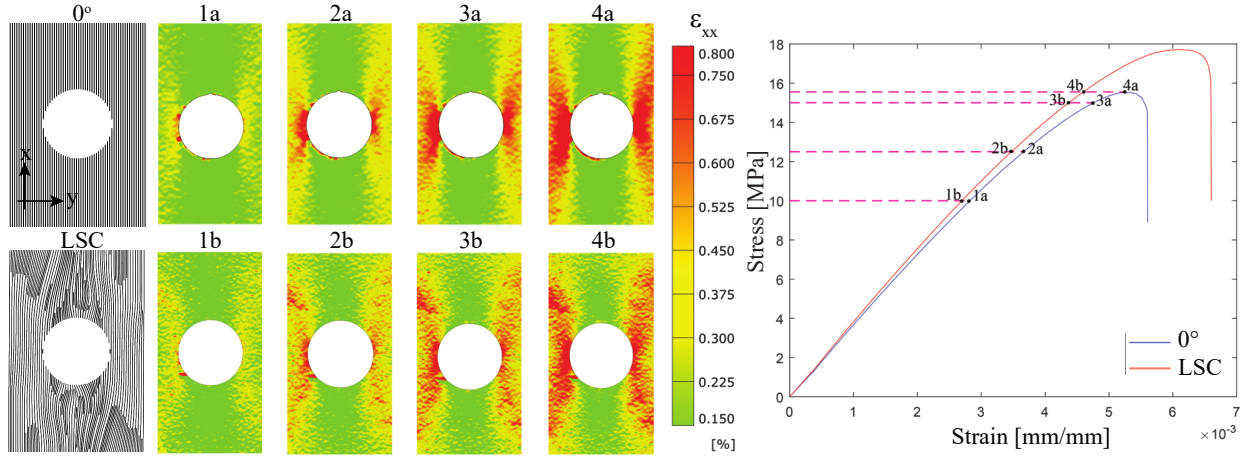


Figure 13: Left: Comparison of DIC strain distributions (ϵ_{xx}) of LSC-design and 0° laminate at four different stress levels; (1a) 0° - 10 MPa, (1b) LSC - 10 MPa, (2a) 0° - 12.5 MPa, (2b) LSC - 12.5 MPa, (3a) 0° - 15 MPa, (3b) LSC - 15 MPa, (4a) 0° - Failure stress of 0°, (4b) LSC - Failure stress of 0°. Right: The corresponding stress-strain curves to DIC measurements; 0° (blue curve) and LSC (red curve).

process and methodology presented in this work could have greater implications to other structural applications and manufacturing processes such as in bi-axial loading case, or a hole geometry with a greater aspect ratio.

Further work on optimization of process condi-

tions is also necessary to minimize defect formation such as optimum choice of nozzle diameter, the use of multiple nozzles with different diameters and/or geometries [60] during manufacturing, more rigorous filament feed-width calculation for curved paths [61], and generation of full continuous paths to avoid mul-

multiple number of start-stop cycles during production of a layer.

The outlined methodology is also translatable to the Automated Fiber Placement (AFP) process for high performance continuous fiber variable stiffness laminate production; however, it should be noted that fiber tow width cannot be varied in AFP as the filament width was varied in this study.

Acknowledgement

The authors would like to acknowledge the support from the teaching scholarship received by Sabanci University, Faculty of Engineering and Natural Sciences for the support of graduate student (TS). Additional thanks go to Isa Emami Tabrizi and Hafiz Qasim Ali for assistance with DIC measurements.

References

- [1] S. F. Kabir, K. Mathur, A.-F. M. Seyam, A critical review on 3d printed continuous fiber-reinforced composites: History, mechanism, materials and properties, *Composite Structures* 232 (2020) 111476.
- [2] S. F. Kabir, K. Mathur, A.-F. M. Seyam, Impact resistance and failure mechanism of 3d printed continuous fiber-reinforced cellular composites, *The Journal of The Textile Institute* (2020) 1–15.
- [3] T. Wieme, D. Tang, L. Delva, D. R. D’hooge, L. Cardon, The relevance of material and processing parameters on the thermal conductivity of thermoplastic composites, *Polymer Engineering & Science* 58 (4) (2018) 466–474.
- [4] G. I. Peterson, M. B. Larsen, M. A. Ganter, D. W. Storti, A. J. Boydston, 3d-printed mechanochromic materials, *ACS applied materials & interfaces* 7 (1) (2014) 577–583.
- [5] S. Mahmood, A. Qureshi, D. Talamona, Taguchi based process optimization for dimension and tolerance control for fused deposition modelling, *Additive Manufacturing* 21 (2018) 183–190.
- [6] H. Prajapati, D. Ravoori, R. L. Woods, A. Jain, Measurement of anisotropic thermal conductivity and inter-layer thermal contact resistance in polymer fused deposition modeling (fdm), *Additive Manufacturing* 21 (2018) 84–90.
- [7] N. van de Werken, H. Tekinalp, P. Khanbolouki, S. Ozcan, A. Williams, M. Tehrani, Additively manufactured carbon fiber-reinforced composites: State of the art and perspective, *Additive Manufacturing* (2019) 100962.
- [8] H. Li, G. Taylor, V. Bheemreddy, O. Iyibilgin, M. Leu, K. Chandrashekhara, Modeling and characterization of fused deposition modeling tooling for vacuum assisted resin transfer molding process, *Additive Manufacturing* 7 (2015) 64–72.
- [9] H. L. Tekinalp, V. Kunc, G. M. Velez-Garcia, C. E. Duty, L. J. Love, A. K. Naskar, C. A. Blue, S. Ozcan, Highly oriented carbon fiber-polymer composites via additive manufacturing, *Composites Science and Technology* 105 (2014) 144–150.
- [10] B. Behdani, M. Senter, L. Mason, M. Leu, J. Park, Numerical study on the temperature-dependent viscosity effect on the strand shape in extrusion-based additive manufacturing, *Journal of Manufacturing and Materials Processing* 4 (2) (2020) 46.
- [11] N. van de Werken, H. Tekinalp, P. Khanbolouki, S. Ozcan, A. Williams, M. Tehrani, Additively manufactured carbon fiber-reinforced composites: State of the art and perspective, *Additive Manufacturing* 31 (2020) 100962.
- [12] S.-H. Ahn, M. Montero, D. Odell, S. Roundy, P. K. Wright, Anisotropic material properties of fused deposition modeling abs, *Rapid prototyping journal* 8 (4) (2002) 248–257.
- [13] C. G. Schirmeister, T. Hees, E. H. Licht, R. Muelhaupt, 3d printing of high density polyethylene by fused filament fabrication, *Additive Manufacturing* 28 (2019) 152–159.
- [14] T. W. Kerekes, H. Lim, W. Y. Joe, G. J. Yun, Characterization of process-deformation/damage property relationship of fused deposition modeling (fdm) 3d-printed specimens, *Additive Manufacturing* 25 (2019) 532–544.
- [15] M. S. Hossain, D. Espalin, J. Ramos, M. Perez, R. Wicker, Improved mechanical properties of fused deposition modeling-manufactured parts

- through build parameter modifications, *Journal of Manufacturing Science and Engineering* 136 (6) (2014) 061002.
- [16] N. Hill, M. Haghi, Deposition direction-dependent failure criteria for fused deposition modeling polycarbonate, *Rapid Prototyping Journal* 20 (3) (2014) 221–227.
 - [17] T. D. McLouth, J. V. Severino, P. M. Adams, D. N. Patel, R. J. Zaldivar, The impact of print orientation and raster pattern on fracture toughness in additively manufactured abs, *Additive Manufacturing* 18 (2017) 103–109.
 - [18] G. D. Goh, Y. L. Yap, S. Agarwala, W. Y. Yeong, Recent progress in additive manufacturing of fiber reinforced polymer composite, *Advanced Materials Technologies* 4 (1) (2019) 1800271.
 - [19] E. Belmonte, M. De Monte, T. Riedel, M. Quaresimin, Local microstructure and stress distributions at the crack initiation site in a short fiber reinforced polyamide under fatigue loading, *Polymer Testing* 54 (2016) 250–259.
 - [20] Z. Jia, T. Li, F.-p. Chiang, L. Wang, An experimental investigation of the temperature effect on the mechanics of carbon fiber reinforced polymer composites, *Composites Science and Technology* 154 (2018) 53–63.
 - [21] L. G. Blok, M. L. Longana, H. Yu, B. K. Woods, An investigation into 3d printing of fibre reinforced thermoplastic composites, *Additive Manufacturing* 22 (2018) 176–186.
 - [22] W. Zhong, F. Li, Z. Zhang, L. Song, Z. Li, Short fiber reinforced composites for fused deposition modeling, *Materials Science and Engineering: A* 301 (2) (2001) 125–130.
 - [23] F. Ning, W. Cong, J. Qiu, J. Wei, S. Wang, Additive manufacturing of carbon fiber reinforced thermoplastic composites using fused deposition modeling, *Composites Part B: Engineering* 80 (2015) 369–378.
 - [24] B. P. Heller, D. E. Smith, D. A. Jack, Planar deposition flow modeling of fiber filled composites in large area additive manufacturing, *Additive Manufacturing* 25 (2019) 227–238.
 - [25] J. R. Raney, B. G. Compton, J. Mueller, T. J. Ober, K. Shea, J. A. Lewis, Rotational 3d printing of damage-tolerant composites with programmable mechanics, *Proceedings of the National Academy of Sciences* 115 (6) (2018) 1198–1203.
 - [26] M. Rouhi, H. Ghayoor, J. Fortin-Simpson, T. T. Zacchia, S. V. Hoa, M. Hojjati, Design, manufacturing, and testing of a variable stiffness composite cylinder, *Composite Structures* 184 (2018) 146–152.
 - [27] A. N. Dickson, D. P. Dowling, Enhancing the bearing strength of woven carbon fibre thermoplastic composites through additive manufacturing, *Composite Structures* 212 (2019) 381–388.
 - [28] K. Sugiyama, R. Matsuzaki, A. V. Malakhov, A. N. Polilov, M. Ueda, A. Todoroki, Y. Hirano, 3d printing of optimized composites with variable fiber volume fraction and stiffness using continuous fiber, *Composites Science and Technology* (2019) 107905.
 - [29] S. Nikbakt, S. Kamarian, M. Shakeri, A review on optimization of composite structures part i: Laminated composites, *Composite Structures* 195 (2018) 158–185.
 - [30] W. Van den Brink, W. Vankan, R. Maas, Buckling-optimized variable stiffness laminates for a composite fuselage window section, *Tech. rep.* (2012).
 - [31] A. Alhajahmad, M. M. Abdalla, Z. Gürdal, Optimal design of tow-placed fuselage panels for maximum strength with buckling considerations, *Journal of Aircraft* 47 (3) (2010) 775–782.
 - [32] J. H. S. Almeida Jr, L. Bittrich, A. Spickenheuer, Improving the open-hole tension characteristics with variable-axial composite laminates: Optimization, progressive damage modeling and experimental observations, *Composites Science and Technology* (2019) 107889.
 - [33] S. Setoodeh, Z. Gurdal, M. Abdalla, L. Watson, Design of variable stiffness composite laminates for maximum bending stiffness, in: 10th AIAA/ISSMO Multidisciplinary Analysis and Optimization Conference, AIAA. doi:10.2514/6.2004-4528.

- [34] R. Groh, P. Weaver, Buckling analysis of variable angle tow, variable thickness panels with transverse shear effects, *Composite Structures* 107 (2014) 482 – 493.
- [35] J. H. S. Almeida Jr, L. Bittrich, E. Jansen, V. Tita, A. Spickenheuer, Buckling optimization of composite cylinders for axial compression: A design methodology considering a variable-axial fiber layout, *Composite Structures* 222 (2019) 110928.
- [36] A. Malakhov, A. N. Polilov, J. Zhang, Z. Hou, X. Tian, A modeling method of continuous fiber paths for additive manufacturing (3d printing) of variable stiffness composite structures, *Applied Composite Materials* (2020).
- [37] M. A. Albazzan, R. Harik, B. F. Tatting, Z. Gürdal, Efficient design optimization of non-conventional laminated composites using lamination parameters: A state of the art, *Composite Structures* 209 (2019) 362 – 374.
- [38] G. Clancy, D. Peeters, V. Oliveri, D. Jones, R. M. O'Higgins, P. M. Weaver, A study of the influence of processing parameters on steering of carbon fibre/peek tapes using laser-assisted tape placement, *Composites Part B: Engineering* 163 (2019) 243 – 251.
- [39] A. W. Blom, M. M. Abdalla, Z. Gürdal, Optimization of course locations in fiber-placed panels for general fiber angle distributions, *Composites Science and Technology* 70 (4) (2010) 564 – 570.
- [40] S. Khan, K. Fayazbakhsh, Z. Fawaz, M. A. Nik, Curvilinear variable stiffness 3d printing technology for improved open-hole tensile strength, *Additive Manufacturing* 24 (2018) 378–385.
- [41] D. M. Peeters, G. G. Lozano, M. M. Abdalla, Effect of steering limit constraints on the performance of variable stiffness laminates, *Computers & Structures* 196 (2018) 94 – 111.
- [42] E. Demir, P. Yousefi-Louyeh, M. Yildiz, Design of variable stiffness composite structures using lamination parameters with fiber steering constraint, *Composites Part B: Engineering* 165 (2019) 733–746.
- [43] Y. Kok, X. P. Tan, P. Wang, M. Nai, N. H. Loh, E. Liu, S. B. Tor, Anisotropy and heterogeneity of microstructure and mechanical properties in metal additive manufacturing: A critical review, *Materials & Design* 139 (2018) 565–586.
- [44] J. R. C. Dizon, A. H. Espera Jr, Q. Chen, R. C. Advincula, Mechanical characterization of 3d-printed polymers, *Additive Manufacturing* 20 (2018) 44–67.
- [45] A. Standard, D5766, standard test method for open-hole tensile strength of polymer matrix composite laminates (2011).
- [46] M. Spoerk, C. Savandaiah, F. Arbeiter, G. Traxler, L. Cardon, C. Holzer, J. Sapkota, Anisotropic properties of oriented short carbon fibre filled polypropylene parts fabricated by extrusion-based additive manufacturing, *Composites Part A: Applied Science and Manufacturing* 113 (2018) 95–104.
- [47] S. G. Advani, C. L. Tucker III, The use of tensors to describe and predict fiber orientation in short fiber composites, *Journal of rheology* 31 (8) (1987) 751–784.
- [48] J. Halpin, J. Kardos, The halpin-tsai equations: a review, *Polymer Engineering & Science* 16 (5) (1976) 344–352.
- [49] G. P. Tandon, G. J. Weng, The effect of aspect ratio of inclusions on the elastic properties of unidirectionally aligned composites, *Polymer composites* 5 (4) (1984) 327–333.
- [50] J. Halpin, J. Karoos, Strength of discontinuous reinforced composites: I. fiber reinforced composites, *Polymer Engineering & Science* 18 (6) (1978) 496–504.
- [51] Y. P. Qiu, G. J. Weng, On the application of Mori-Tanaka's theory involving transversely isotropic spheroidal inclusions, *Int. J. Eng. Sci.* 28 (11) (1990) 1121–1137.
- [52] T. Shafighfard, E. Demir, M. Yildiz, Design of fiber-reinforced variable-stiffness composites for different open-hole geometries with fiber continuity and curvature constraints, *Composite Structures* (2019) 111280.
- [53] J. Minardi, Mecode: GCode for all - Python Module (2020).
URL <https://github.com/jminardi/mecode>

- [54] S. Hartmann, A. K. Marghzar, Modeling of fiber circumplacement around a hole using a stream-line approach, *Universal Journal of Mathematics and Applications* 1 (1) (2018) 17–28.
- [55] K. Gliesche, T. Hübner, H. Orawetz, Application of the tailored fibre placement (tfp) process for a local reinforcement on an “open-hole” tension plate from carbon/epoxy laminates, *Composites Science and Technology* 63 (1) (2003) 81–88.
- [56] M. Tosh, D. Kelly, On the design, manufacture and testing of trajectorial fibre steering for carbon fibre composite laminates, *Composites Part A: Applied Science and Manufacturing* 31 (10) (2000) 1047–1060.
- [57] X. Niu, T. Yang, Y. Du, Z. Xue, Tensile properties of variable stiffness composite laminates with circular holes based on potential flow functions, *Archive of Applied Mechanics* 86 (9) (2016) 1551–1563.
- [58] P. M. Gerhart, A. L. Gerhart, J. I. Hochstein, Munson, Young and Okiishi’s Fundamentals of Fluid Mechanics, Binder Ready Version, John Wiley & Sons, 2016.
- [59] L. Drzal, M. Madhukar, Fibre-matrix adhesion and its relationship to composite mechanical properties, *Journal of Materials Science* 28 (3) (1993) 569–610.
- [60] B. Akhouni, A. H. Behraves, A. B. Saed, An innovative design approach in three-dimensional printing of continuous fiber-reinforced thermoplastic composites via fused deposition modeling process: In-melt simultaneous impregnation, *Proceedings of the Institution of Mechanical Engineers, Part B: Journal of Engineering Manufacture* 234 (1-2) (2020) 243–259.
- [61] B. Akhouni, M. Nabipour, F. Hajami, S. S. Band, A. Mosavi, Calculating Filament Feed in the Fused Deposition Modeling Process to Correctly Print Continuous Fiber Composites in Curved Paths, *Materials (Basel)*. 13 (20) (2020) 4480.